

This manuscript has been authored by UT-Battelle, LLC, under contract DE-AC05-00OR22725 with the US Department of Energy (DOE). The US government retains and the publisher, by accepting the article for publication, acknowledges that the US government retains a nonexclusive, paid-up, irrevocable, worldwide license to publish or reproduce the published form of this manuscript, or allow others to do so, for US government purposes. DOE will provide public access to these results of federally sponsored research in accordance with the DOE Public Access Plan (<http://energy.gov/downloads/doe-public-access-plan>).

## Effects of Lead and Lean in Multi-Axis Directed Energy Deposition

**Omar Elsayed<sup>a</sup>**

E-mail: [oelsayed791@gatech.edu](mailto:oelsayed791@gatech.edu)

Correspondence E-mail: [oelsayed791@gmail.com](mailto:oelsayed791@gmail.com)

**Samuel Kersten<sup>a</sup>**

E-mail: [skersten3@gatech.edu](mailto:skersten3@gatech.edu)

**Derek Vaughan<sup>a</sup>**

E-mail: [dvaughan3@gatech.edu](mailto:dvaughan3@gatech.edu)

**Christopher Masuo<sup>a</sup>**

E-mail: [cmasuo3@gatech.edu](mailto:cmasuo3@gatech.edu)

**Karthik Adapa<sup>a</sup>**

E-mail: [karthik.adapa@gatech.edu](mailto:karthik.adapa@gatech.edu)

**Myong Joon Kim<sup>a</sup>**

E-mail: [mkim3@gatech.edu](mailto:mkim3@gatech.edu)

**Thomas Feldhausen<sup>b</sup>**

E-mail: [feldhausenta@ornl.gov](mailto:feldhausenta@ornl.gov)

**Christopher Saldana<sup>a</sup>**

E-mail: [christopher.saldana@me.gatech.edu](mailto:christopher.saldana@me.gatech.edu)

**Thomas Kurfess<sup>a</sup>**

E-mail: [kurfess@gatech.edu](mailto:kurfess@gatech.edu)

<sup>a</sup> *George W. Woodruff School of Mechanical Engineering, Georgia Institute of Technology, 801 Ferst Dr, Atlanta, GA 30332*

<sup>b</sup> *Manufacturing Automation and Controls Group, Oak Ridge National Laboratory, Oak Ridge, TN 37831*

**ABSTRACT.** *The present study examines the effect of varying laser incidence angles on textural, microstructural, and geometric characteristics of directed energy deposition (DED) processed materials, providing a more comprehensive outlook on participating laser-matter interaction phenomena and ultimately devise strategies to ameliorate print performance. In this study, single-layer, single-/multi-track specimens were processed to examine the effect of non-orthogonal angular configurations on bead morphology, microstructure, phase composition and textural representation of DED-processed 316L stainless steel materials. It was observed that bead size decreased at increasing lead and lean angles. Asymmetry in the distribution of the bead morphology as a function of lead angle indicates better catchment for acute lead angle configurations over obtuse configurations. No significant differences in phase composition, texture, and microstructure were observed in moderate off-axis configurations. When penetration depth for the deposits was below 20  $\mu\text{m}$ , columnar structures dominated the microstructure of the*

*deposited material. At deeper penetration depths, columnar and equiaxed structures were observed at the bead-substrate interface and center of the bead, respectively. Compared to powder-blown DED, wire-DED dilution profiles were found to be asymmetric in both orthogonal and non-orthogonal wire DED samples.*

**Keywords:** *Directed energy deposition, additive manufacturing, microstructure*

## 1 Introduction

Hybrid manufacturing is an emerging technology that incorporates both additive and subtractive manufacturing (AM and SM, respectively) in producing net-shape components, yielding advantages that neither technology can supply when used in isolation [1, 2, 3]. By combining additive and subtractive capabilities, components with complex geometries can be manufactured and post-processed to produce dimensional accuracies and surface finishes that are unmatched by using current additive or subtractive technologies alone, all in one unified machine [4, 5]. Complex geometries produced by hybrid manufacturing generally require use of off-axis tool orientation (e.g., lead and lean) to accommodate reach and access to manufacture specific component geometry. When dealing with highly intricate geometries in hybrid manufacturing, the issues that arise due to tool reachability and access in both additive and subtractive steps of the process become significant, increasing the probability of tool crashing dramatically.

The impact of off-axis deposition orientation in DED has not been well established. In DED, a conical nozzle outputs powder at an angle, allowing powder to meet the focused laser beam at the workpiece surface. During deposition, however, not all the deposited powder is melted; rather, random, and turbulent rebounding of the powder particles results in a powder cloud [6]. As these particles get exposed to the laser beam, they absorb and/or reflect some of the laser energy [7]. In low-melting and boiling-point alloy deposition, vapor plumes exacerbate this optical obstruction [8]. As a result, the effective laser energy used to create the melt pool is lower than intended. This is referred to as laser attenuation and can result in considerable efficiency losses. The laser incidence angle can have a direct effect on the extent of laser attenuation and can be strategically employed to reduce efficiency losses that are endemic to more extreme process parameters. Various theoretical models and experimental validations were conducted to analyze the effects laser attenuation has on deposition performance when laser incidence angle is varied. Fu et al. developed a theoretical model where it was observed that increasing angle between the laser and powder jet incident angles resulted in more asymmetric temperature distributions as well as lower average temperatures due to the reduced travel experienced by the particles within the laser field [9]. It was also observed that laser attenuation increased on decreasing angles between laser and powder jet incidence angle, resulting in upwards of 50% effective power losses and transforming the power distribution from Gaussian to non-Gaussian in nature. Liu et al. have also shown that laser attenuation is enhanced with increasing particle feed rate and particle speed, with up to 10% efficiency losses [10]. Pinkerton et al. found that laser attenuation becomes significantly more pronounced once the powder streams converge to form a single stream at the center [11]. The laser incidence angle can also directly affect the resultant print bead morphologies. Hao et al. [12] observed that an increasing laser to substrate angle (lead angle) results in an increasing bead width and peak point shifting. This was attributed to the presence of gravitational effects and/or changes in spot size and geometry.

There have been various efforts to examine the effect of laser incidence angles on printing performance, including characteristics such as bead geometry and laser power/surface temperature

distributions, amongst others [10, 11, 12]. However, limited work has been conducted on examining the effect of laser incidence angles on bead texture and microstructure. Furthermore, no work has been done to relate such domains with bead geometry, laser attenuation, or other participating physical phenomena to provide a more holistic understanding of some underlying laser-matter interaction phenomena in directed energy deposition processes. To address this need, the present study seeks to understand the impact of laser incidence angle in DED on bead morphology, microstructure, and texture, as well as the nature of its effects. In addition, a comparison study is also required to understand the impact of laser incidence angle in the powder feed against wire feed DED methods. Typically, a wire DED system has nearly 100% feedstock catchment efficiency, significantly higher than the powder feed system due to no bombardment of powder particles. With an expectation that wire feed DED exhibits a prominent trend, a similar microstructural characterization study including the bead morphology is investigated to assess and understand the similarities between powder and wire feed DED systems.

## 2 Experimental Procedure

Powder blown DED was employed to perform the required experiments in this study using the Mazak VC-500AM hybrid machine. The powder material of choice was 316L austenitic stainless steel (sourced from LPW Technology Limited, a Carpenter Company). The 316L powder material was deposited on a 316L substrate with a thickness of 6.35 mm and the chemical composition of the powder material is provided in Table 1. The particle size distribution of the powder used in this study was within 45-106  $\mu\text{m}$ , per the sieve analysis conducted following ASTM-B214. The process parameters used in this experimentation were kept constant to isolate the effects of incidence angle on phase composition, texture, bead morphology, and microstructure. Table 2 illustrates the parameters used for this process.

**Table 1. 316L Austenitic Stainless-Steel Chemical Composition (wt%) (Sourced from LPW Technology Limited, a Carpenter Company)**

Fe	Cr	Ni	Mo	Mn	Si	N	C	Cu	O	P	S
Bal.	17.8	13.0	2.40	1.04	0.64	0.1	0.02	0.02	0.01	0.01	0.004

**Table 2. Powder-Feed DED Process Parameters**

Parameter	Value
Scanning Speed (mm/min)	300
Laser Power (W)	400
Nozzle Gas Flowrate (L/min)	2
Shielding Gas Flowrate (L/min)	10
Carrier Gas Flowrate (L/min)	5
Powder feed rate (g/min)	4.6

The angle between the laser head vertical axis and the workpiece surface is known as the laser incidence angle. In terms of deposition, there are two types of incidence angles: lead and

lean. The lead angle is the angle produced in the YZ plane (also known as the tilt angle [12]), while the lean angle is the angle produced in the XZ plane (assuming the laser travels in the Y-direction). In general, there are four main configurations possible: orthogonal, pure lean/lead, and compound lean/lead angles. Figure 1 visually illustrates the differences between the various angular configurations discussed here. The yellow line represents the laser beam, while the coordinate system shown is that of the substrate.

A total of 5 experiments were conducted in this study. The first experiment examined pure lead, pure lean, compound, and orthogonal angle effects on bead geometry. A set of 5 in long single-layer, single track depositions are conducted for each configuration. The various angular configurations examined are shown in Table 3. The samples are deposited approximately 5 mm apart to prevent heat-affected zone (HAZ) overlapping, which can interfere with the melt-pool and solidification dynamics as well as the resultant microstructure of the deposits. A single-layer track was employed to avoid altering melt-pool behaviors and introducing secondary effects of vertical inter-layer diffusion and solidification phenomena, therefore convoluting the primary results of this study. After deposition, the samples were sectioned and mounted for metallographic examination to examine bead geometry via optical microscopy. Five samples of each configuration were obtained. A 3:2:1-part solution of distilled water, hydrochloric acid, and nitric acid are used to reveal the bead cross-sections here (Solution 88 from ASTM E407-99). The evaluation metrics in this experiment were bead height, bead width, and penetration depth (the maximum distance penetrated by the laser to induce dilution in the substrate).

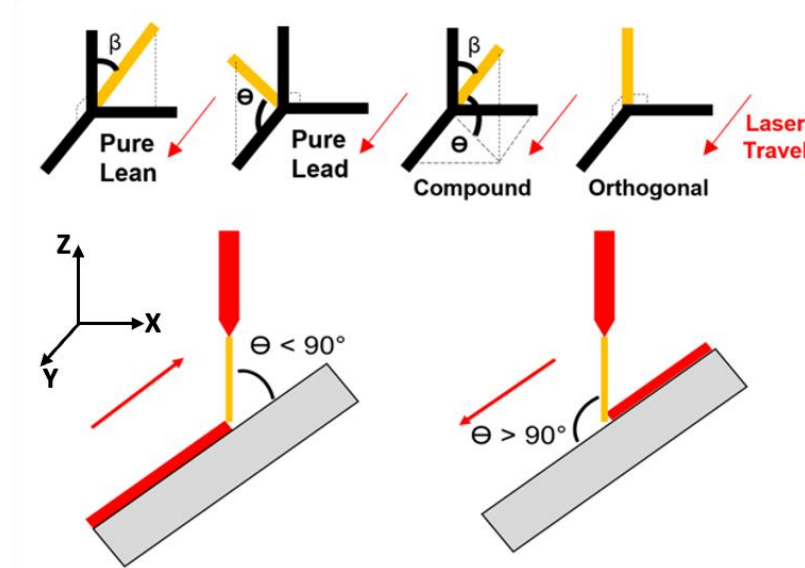


**Figure 1.** Top: Orthogonal and non-orthogonal angle representations. Bottom: Lead angle deposition techniques.

**Table 3. Experiment 1 Angular Configurations**

Configuration	Lead Angle - $\Theta$ (°)	Lean Angle - $\beta$ (°)
Orthogonal	90	0
Pure Lean	90	15, 30
Pure Lead	45, 60, 75, 105, 120, 135	0
Compound	45, 60, 75, 105, 120, 135	15, 30

The second experiment focused on determining differences in phase composition and texture between non-orthogonally (pure lead configurations of  $\Theta = 60^\circ$  and  $120^\circ$ ) deposited material, orthogonally deposited material, and the raw, unprocessed powder. In this experiment, three 1 in x 0.5 in, single-layer, multi-track samples were produced: a sample with an orthogonal configuration and two samples with pure lead angles of  $\Theta = 60^\circ$  and  $120^\circ$ . A single-layer track was employed to avoid altering melt-pool behaviors and introducing secondary effects of vertical inter-layer diffusion and solidification phenomena, therefore convoluting the primary results of this study. A multi-track deposit was necessary due to spot size limitations set forth by the X-ray equipment utilized in this experiment. Phase analysis was conducted on all three samples as well as the raw, unprocessed powder to provide a comparative basis on the processing effects on phase composition. Textural analysis was then conducted to obtain orientation distribution functions (ODF) to map the textural demographics present in the samples. The orientation distribution functions provide a global representation of texture within a large area of a sample, thus providing a higher-level view of the crystallographic orientations in the investigated samples.

The third experiment examined pure lead, pure lean, and compound angle effects on microstructure. A set of 1 in single-track, single-layer samples with various angular configurations was deposited, as shown in Table 4. They were then sectioned and prepared for detailed microstructural analysis. The samples were etched using the same etching solution described in the first experiment. The grain size was also examined in 7 100  $\mu\text{m}$  by 100  $\mu\text{m}$  regions that cover the entirety of the bead, as shown by the green boxes in Figure 2. Five straight, horizontal lines were drawn at equal intervals within the square region, and the line intercept method was used [13]. Grain sizes are then compared both between regions within a bead and across beads. Furthermore, a set of 4 samples of extreme non-orthogonal deposition angles was also investigated to examine the effect of extreme non-orthogonal, compound angle deposition on bead microstructure. The goal was to examine the effects at the upper and lower bounds of the hybrid machine regarding non-orthogonal deposition to further complement the results of the first experiment. The angular configurations examined here are presented in Table 4.

**Table 4. Experiment 3 Angular Configurations**

Configuration	Lead Angle - $\Theta$ (°)	Lean Angle - $\beta$ (°)
Orthogonal	90	0
Pure Lean	90	15
Pure Lead	75, 105	0
Compound	75, 105	15
Upper & Lower Bounds	45, 135	15, 45

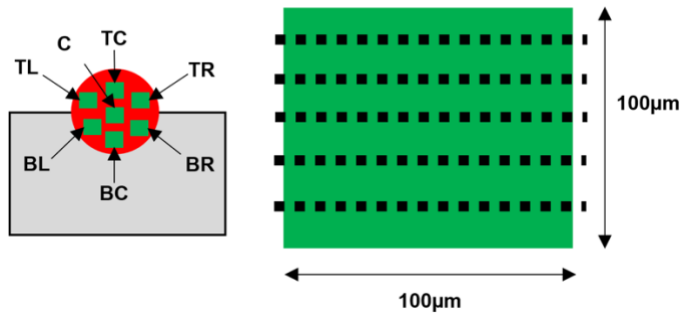


**Figure 2.** Lead angle effects on bead microstructure experimental setup. Left: Cross sectional area to be investigated metallographically. L = left, C = center, TC = top center, TR = top right, BL = bottom left, BC = bottom center, BR = bottom right. Right: examined region for the manual intercept method setup

The fourth experiment involved using a Macken Instruments P-2000Y laser power probe to quantitatively measure the effects of varying incidence angles on the effective power reaching the substrate surface [14]. All angular configurations examined in the first experiment were investigated here, as is denoted in Table 1. A stand-off distance of 33 mm was maintained to ensure the laser spot size was larger than the minimum manufacturer recommendation of 1.09 cm to prevent equipment damage. The power probe was exposed to the laser beam for 21 s per run, as per manufacturer instructions. To accomplish this, the probe is rotated in such a way that a full rotation is complete in 21 s. The circular trajectory of the laser beam has a diameter of 31 mm so that the linear travel speed matches the regular deposition runs from the first experiment, at 300 mm/min. The experiments are run with the powder feed on and off to attempt at decoupling laser spot size and powder attenuation effects, respectively. Figure 3 illustrates the experimental setup used here. The power absorbed by the power meter (termed the effective power here) was compared to the command power (set at 400 W for this study) to obtain the difference in power, representing the power loss experienced as the laser travels to the substrate.

$$P_{\text{effective}} = P_{\text{command}} - P_{\text{attenuated}}$$

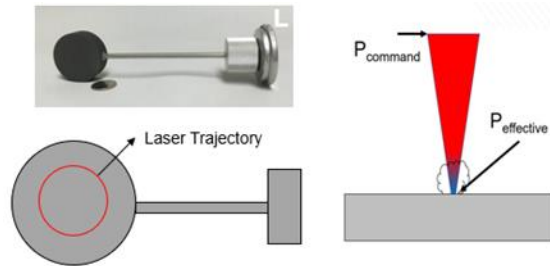


**Figure 3.** Laser Power Measurement Experimental Setup (Top right figure obtained from the manufacturer's website [L]).

Finally, the fifth experiment involves conducting a comparative study using the Mazak VC-500A/5X AM HWD system to compare the non-orthogonal deposition performance of powder-feed and wire-feed hybrid AM systems. The specific lean and lead angles examined in this experiment are shown in Table 5. The wire-fed samples are processed using a 3-kW continuous wave (CW) laser. A 0.045 in (1.14 mm) 316L SS wire was used as the wire gauge and material of choice, respectively. The process parameters used are summarized in Table 6. Optical microscopy was then employed to examine geometric and microstructural characteristics of the resultant bead cross-sections. More specifically, bead height, width, penetration depth, and grain structure are studied.

**Table 5. Experiment 5 Angular Configurations**

Angular Configuration	Lead Angle - $\Theta$ (°)	Lean Angle - $\beta$ (°)
Orthogonal	90	0
Pure Lean	90	15, 30, 40
Pure Lead	60, 75, 90, 105, 130	0

**Table 6. Wire-Feed DED Process Parameters**

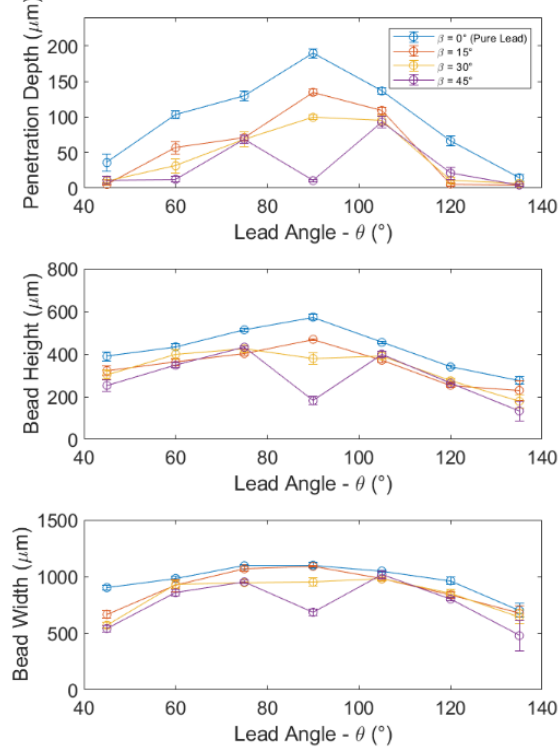
Process Parameter	Value
Laser Spot Diameter (mm)	3
Scanning Speed (mm/min)	1067
Laser Power (W)	2750
Nozzle Gas Flowrate (L/min)	20
Shielding Gas Flowrate (L/min)	20
Wire Feed Speed (mm/min)	4445
Hot Wire Power (W)	420

### 3 Results

#### 3.1 Effects of lead and lean angles in blown powder DED

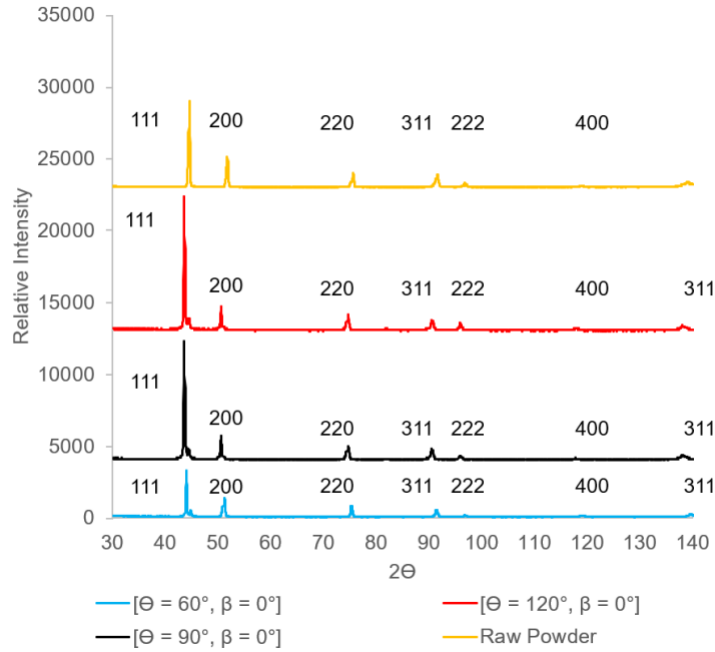
Figure 4 illustrates the resultant bead widths, heights, and penetration depths of the various angular configurations examined. From the figure, an increase in lean angle resulted in diminished penetration depth, bead height and bead width, irrespective of the lead angle utilized. Penetration depth experienced a more significant drop with a 75° lead angle as compared to a 105° lead angle. However, with more extreme lead angles, obtuse lead angle penetration depths decreased more significantly with penetration depths highly dependent on a lean angle here, as observed by the spread in the data. Another observable asymmetry can be seen in the bead height changes, where bead height was lower in lead angle configurations higher than 90° for all lean angles used compared to their mirror equivalents under 90°. Regarding bead width, slight asymmetry was observed when comparing acute and obtuse lead angles, with acute lead angle bead widths having

slightly higher values than obtuse lead angle bead widths, especially for lower lean angle compound configurations. Interestingly, across all bead parameters examined, incorporating a pure lean angle of 45° resulted in a pronounced drop in bead height, width, and penetration depth as compared to its compound angle counterparts.



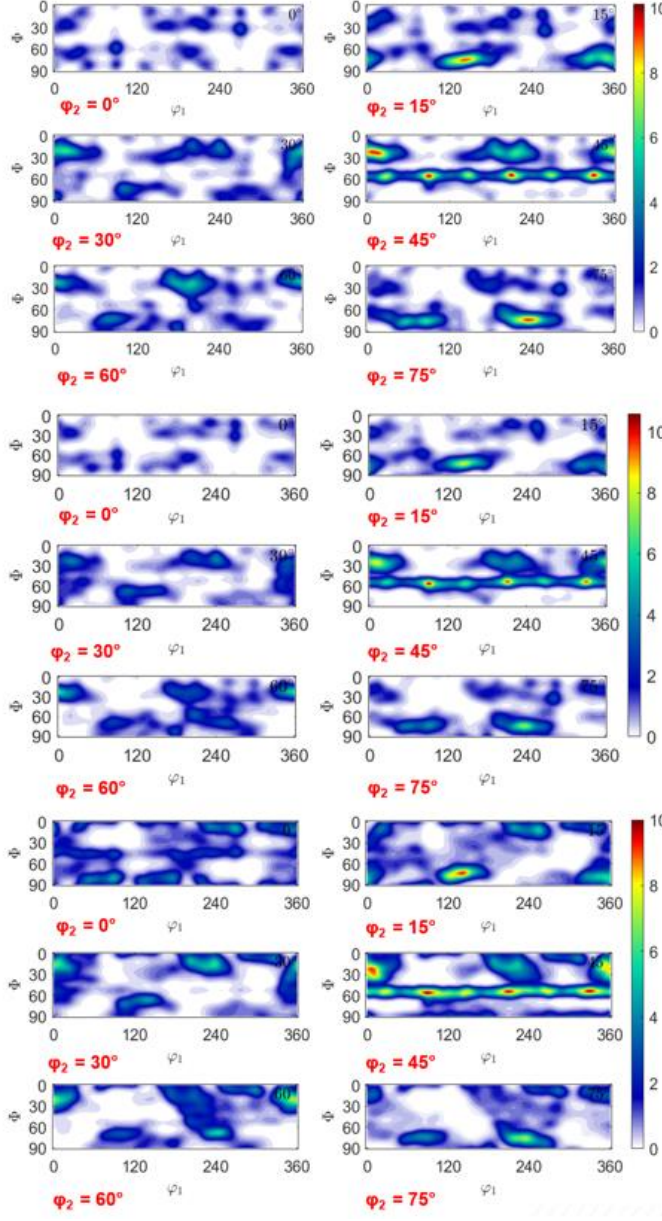
**Figure 4.** Lean and lead angles effects on bead morphology. Normal curve behavior with more extreme lead angles. Diminishing parameters with more extreme lean angles.

Figure 5 illustrates the X-ray diffraction peaks of the non-orthogonal and orthogonal configurations as well as that of the unprocessed powders. The diffraction peaks were overlaid for ease of visualization. The material candidates that matched the unprocessed and processed samples (C-Cr-Fe-Ni and CFe<sub>15.1</sub>) were austenitic FCC phases. From the figure, no relative differences were detected in peak locations. The qualitative austenitic FCC phase determination was sufficient for subsequent analyses, which were highly dependent on the h-k-l values representative of the detected peaks at lower angles.



**Figure 5.** X-ray diffraction peak patterns. Yellow: raw, unprocessed powder. Red:  $\Theta = 120^\circ$  pure lead condition. Black: orthogonal sample. Blue:  $\Theta = 60^\circ$  pure lead condition. No significant differences in phases were observed.

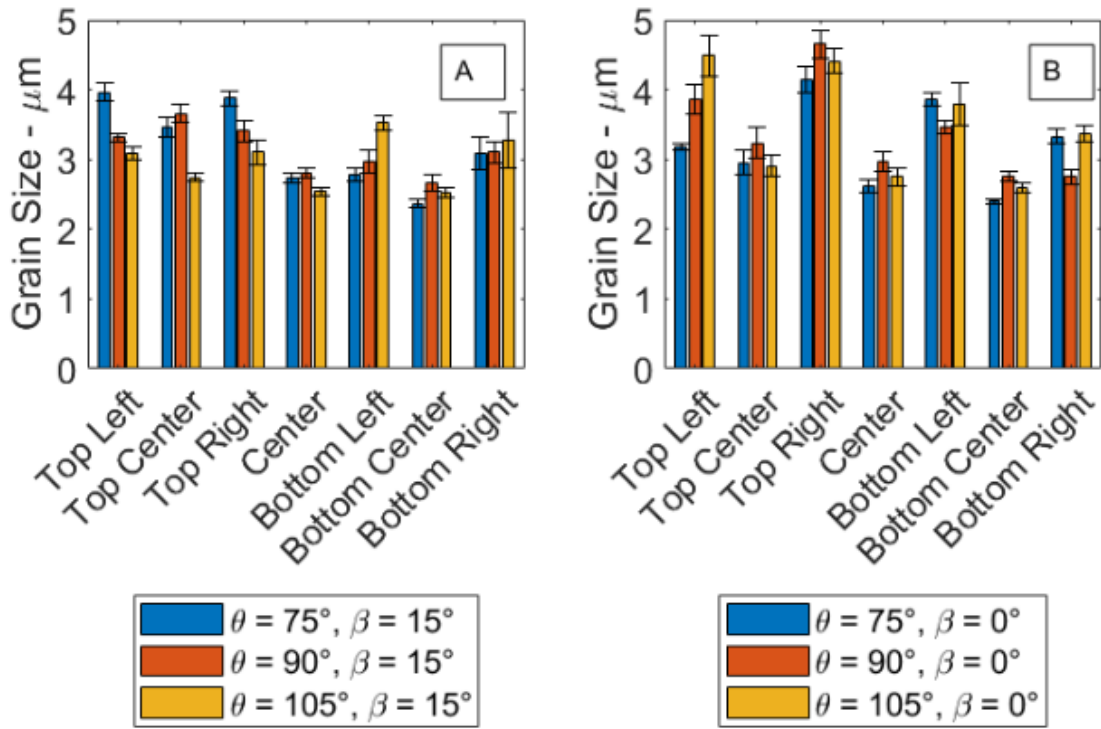
Figure 6 illustrates the calculated orientation distribution functions of the non-orthogonal and orthogonal processed samples. From the texture measurements conducted, it was observed that similar textural representations were present in orthogonal and non-orthogonal samples. The significant texture was observed at  $\varphi = 60^\circ$ ,  $\varphi_2 = 45^\circ$ , and all  $\varphi_1$  values for all the samples, indicating that fiber texture is dominant in this specific orientation. Furthermore, high texture intensities were observed in the  $\varphi_2 = 15^\circ$  and  $\varphi_2 = 75^\circ$  plots around  $\varphi = 75^\circ$  in various  $\varphi_1$  angles, as observed in the figures. The remaining areas in the ODFs exhibited little texture elsewhere, confirming that a significant textural representation is indeed present, as observed by the high intensity counts in the diffraction patterns in Figure 5.



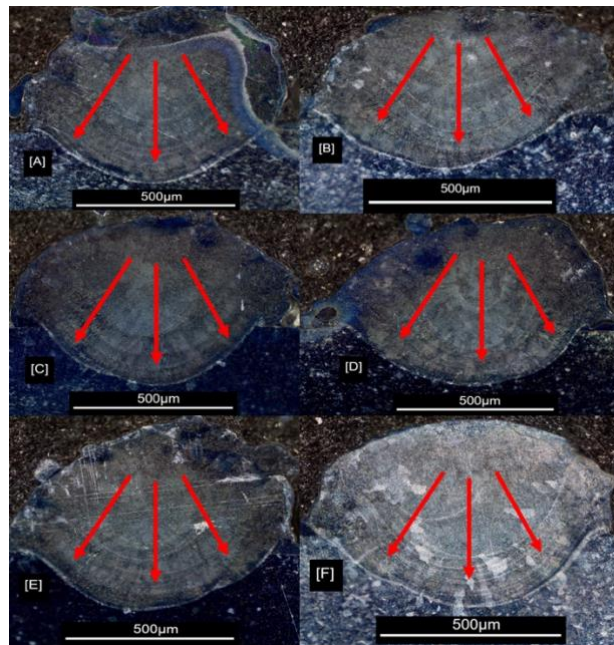
**Figure 6.** Orientation distribution function plots. Top:  $\Theta = 60^\circ$ ,  $\beta = 0^\circ$ . Middle:  $\Theta = 90^\circ$ ,  $\beta = 0^\circ$ . Bottom:  $\Theta = 120^\circ$ ,  $\beta = 0^\circ$ . No significant differences in textural representation between samples.

Figure 7 illustrates the grain size differences between the various regions within a specific sample and across different samples for pure lead angle and pure lean/compound angle configurations. The data is divided into two plots: a pure lead condition ( $\beta = 0^\circ$ ) and a compound condition ( $\beta = 15^\circ$ ). All seven regions selected to examine the microstructure within each plot are illustrated and separated from each other as shown. Within each region of the plots, the various angular configurations are situated side-by-side for an easy-to-visualize comparison. As observed in Figure 7, minor microstructural grain size variations were observed with changing lead and lean combinations, across samples, with variations not exceeding  $1-1.5 \mu\text{m}$ . Furthermore, variations between neighboring regions within a sample did not exceed  $2-2.5 \mu\text{m}$ . Nevertheless, the grains

nearest to the center were slightly smaller than on the outer edges of the bead. Figure 8 illustrates the micrographs obtained from pure lean, pure lead, compound, and orthogonal angular configurations. Similar solidification fronts were observed in all samples. They all exhibited a radial symmetry which originated in the top center region of the beads. Columnar structures were detected at the outer edges of the bead, more specifically at the bead-substrate interface, while more equiaxed and cellular structures were observed closer to the center of the beads, as shown in Figure 9. For beads with very shallow penetration depths ( $< 20 \mu\text{m}$ , more apparent in more extreme lead angles of  $45^\circ$  and  $60^\circ$ , as shown in Figure 4), columnar structures dominated the general microstructure, with little to no equiaxed or cellular structures present. This is depicted in Figures 9 and 10.



**Figure 7.** Pure lead, lean and compound angle effects on grain size. [A] Pure lean (red) and compound (blue and yellow) angular configurations . [B] Pure lead (blue and yellow) and orthogonal (red) angular configurations. Negligible differences both between regions within a single bead and across beads for varying laser incidence angles.



**Figure 8.** Micrographs of orthogonal and non-orthogonal solidification fronts. [A]  $\Theta = 75^\circ$ ,  $\beta = 0^\circ$ . [B]  $\Theta = 90^\circ$ ,  $\beta = 0^\circ$ . [C]  $\Theta = 105^\circ$ ,  $\beta = 0^\circ$ . [D]  $\Theta = 75^\circ$ ,  $\beta = 15^\circ$ . [E]  $\Theta = 90^\circ$ ,  $\beta = 15^\circ$ . [F]  $\Theta = 105^\circ$ ,  $\beta = 15^\circ$ . Equivalent solidification fronts observed.

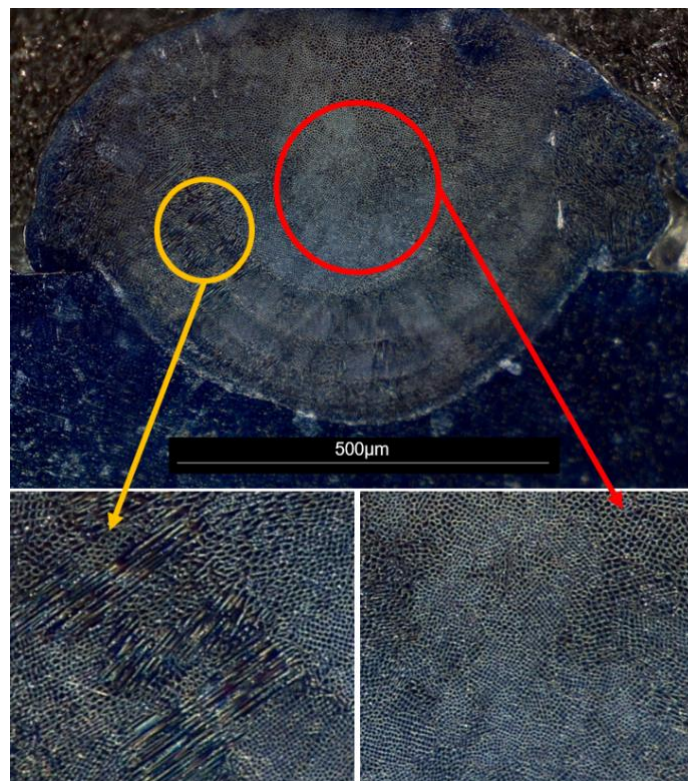


**Figure 9.** Grain morphology representation in orthogonal and non-orthogonal bead depositions. Yellow: Columnar structures. Red: Equiaxed/cellular structures.

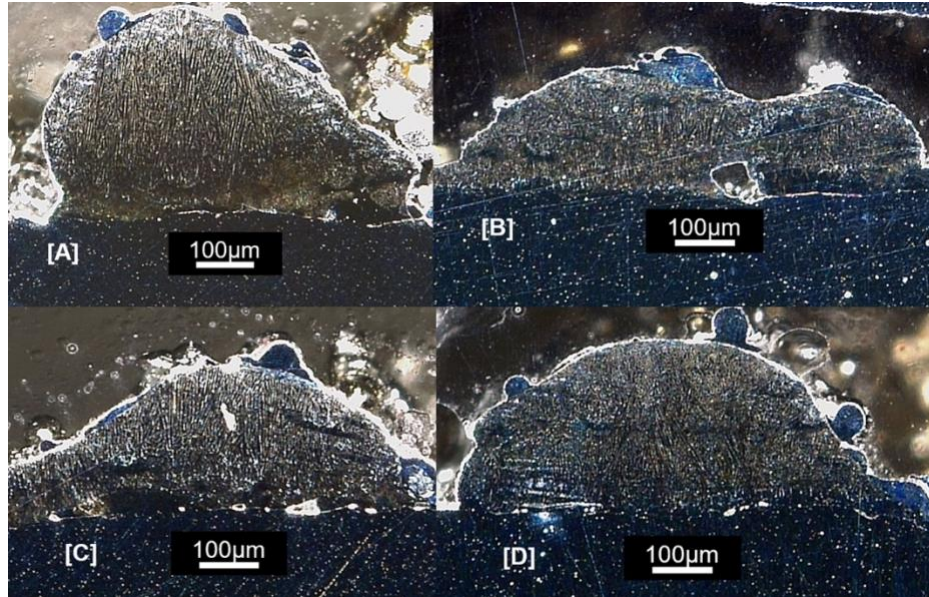


**Figure 10.** Grain morphology representation of bead depositions with penetration depths  $<20\mu\text{m}$ .  
 [A]  $\Theta = 45^\circ$ ,  $\beta = 15^\circ$ . [B]  $\Theta = 135^\circ$ ,  $\beta = 15^\circ$ . [C]  $\Theta = 45^\circ$ ,  $\beta = 45^\circ$ . [D]  $\Theta = 135^\circ$ ,  $\beta = 45^\circ$ .  
 Columnar structures dominate beads with shallow penetration depths.

Figure 11 illustrates the laser power measurements obtained from this experiment. A dioptric power loss of approximately 25-50W, representing a 6.25% to 12.5% drop from the command power of 400W, was observed when the machine was operated with the powder feed turned off. Regarding the effect of varying the incidence angles, the consequential laser spot size changes that were experienced did not have a specific effect on the amount of power reaching the probe surface. No observable trend was seen in the obtained results, with most data points lying within a 25W range between 350W and 375W. The measured power was, on average, approximately  $362.5 \pm 12.5$  W for all measured incidence angle combinations. When the powder feed was turned on, the measured laser power dropped an additional 25-50W, resulting in an 18.75% to 25% overall drop from the command power of 400W. When the powder feed was off, changing the laser incidence angle configuration did not significantly affect the power measured/absorbed by the probe. The measured power here was, on average, approximately  $315 \pm 10$  W for all measured incidence angle combinations.

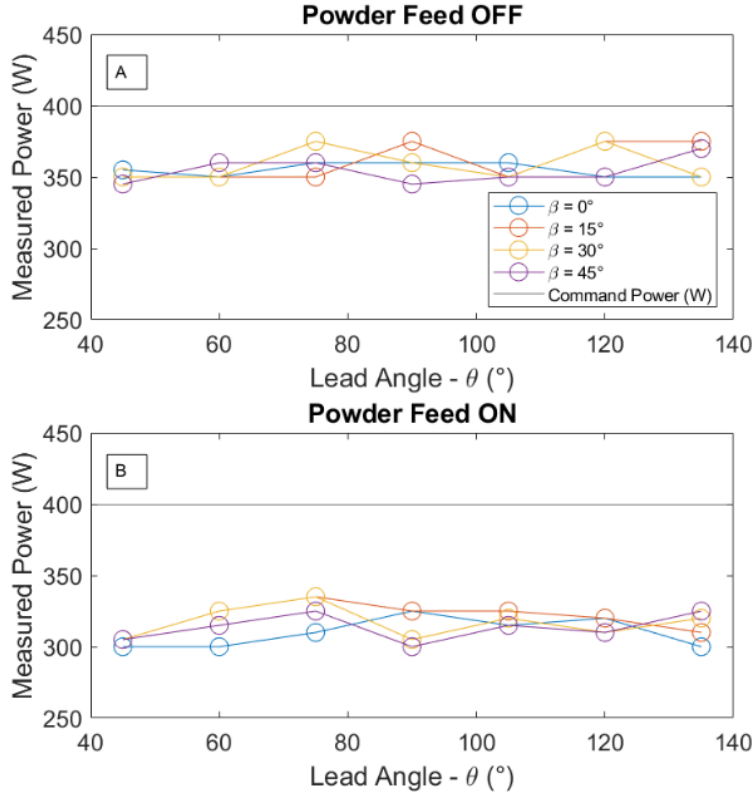


**Figure 11.** Laser attenuation quantitative measurements. [A] Powder feed turn off. [B] Powder feed turn on. There are slight differences between varying laser incidence angles with powder feed turned ON and OFF. Laser attenuation is more pronounced when the powder feed is turned ON as compared to when it is turned OFF, though.

### 3.2 Effects of lead and lean angles in wire-fed DED

Figure 12 illustrates the bead cross-sectional micrographs obtained from the pure lead (A, B, D, E), pure lean (F, G, H), and orthogonal (C) angle depositions in the wire feed DED case. Figures 12A to 12H show that the dilution region is asymmetrically positioned away from the bead center. In pure lead angle configurations (except for  $[\Theta = 105^\circ, \beta = 0^\circ]$  in 12D), the dilution region was preferentially positioned to the right of the bead center, with no significant variations in position with increasing lead angles. In pure lean angle configurations, the dilution region was preferentially positioned to the left of the bead center, progressively shifting to the right with increasing lean angle. An asymmetry was also observed in the orthogonal configuration. As compared to other angular configurations, the  $[\Theta = 105^\circ, \beta = 0^\circ]$  pure lead angle configuration (Figure 12D) exhibited a much smaller and distinctive penetration depth profile. Maximum penetration was observed towards the bead extremities (compared to a preferentially centered, though asymmetric location for other angular configurations).

The relation between angular configuration and bead geometry (bead height, width, and penetration depth) is illustrated in Figure 13. It can be observed in Figures 13A and 13B that height and penetration depth followed an inverse Bell curve relationship with increasing lead angles. On the other hand, Figure 13C shows that bead width exhibits a normal Bell curve behavior. A noticeable asymmetry in bead geometry changes due to angular configuration can be observed in lead angles lower than  $105^\circ$  as compared to lead angles larger than  $105^\circ$ . Penetration depth and bead height exhibit a Bell curve behavior, with maximum penetration depth and maximum bead

height experienced at  $\beta = 30^\circ$  and  $\beta = 15^\circ$ , respectively. Bead width experiences an inverse Bell curve behavior, with the minimum width experienced at  $\beta = 15^\circ$ . At  $\beta = 40^\circ$ , a significant jump in bead width was experienced.

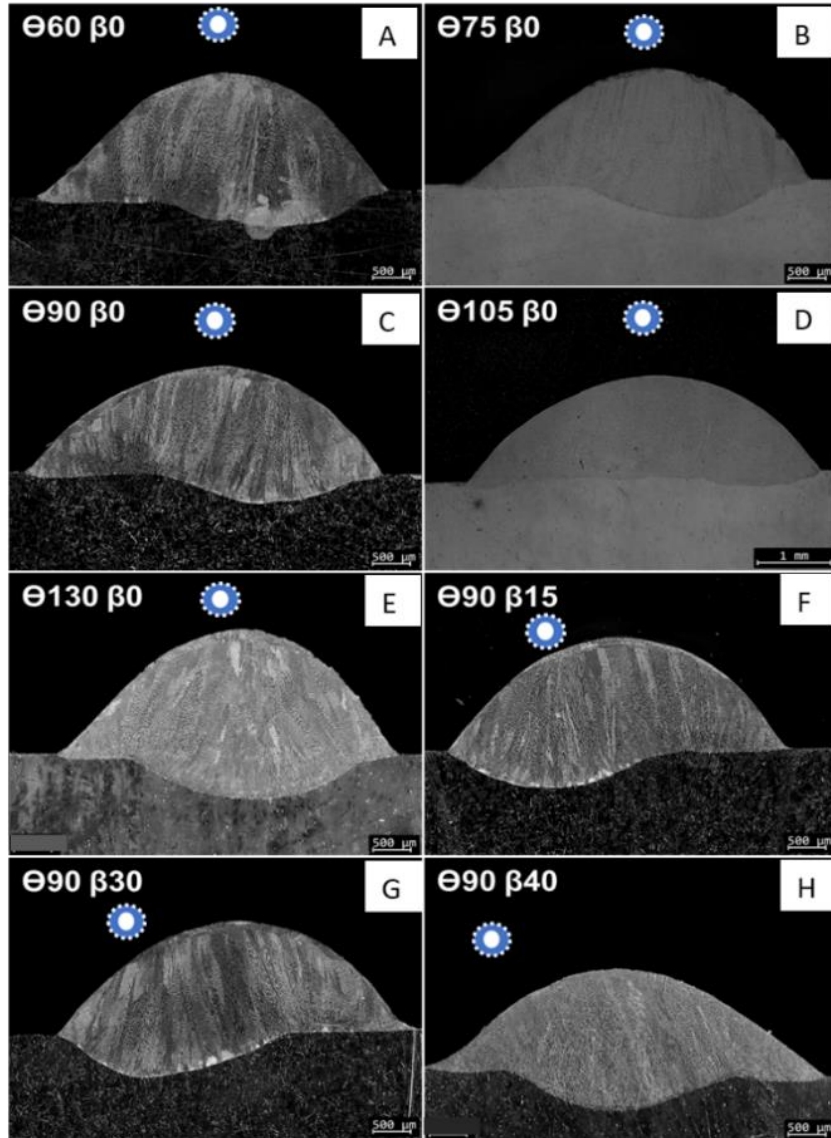


**Figure 12.** Micrographs of wire-feed DED samples, where [A]  $\Theta = 60^\circ$ ,  $\beta = 0^\circ$ . [B]  $\Theta = 75^\circ$ ,  $\beta = 0^\circ$ . [C]  $\Theta = 90^\circ$ ,  $\beta = 0^\circ$ . [D]  $\Theta = 105^\circ$ ,  $\beta = 0^\circ$ . [E]  $\Theta = 130^\circ$ ,  $\beta = 0^\circ$ . [F]  $\Theta = 90^\circ$ ,  $\beta = 15^\circ$ . [G]  $\Theta = 90^\circ$ ,  $\beta = 30^\circ$ . [H]  $\Theta = 90^\circ$ ,  $\beta = 40^\circ$ . Dotted and solid circles represent the position of laser and direction of wire-feed for corresponding angular setting.

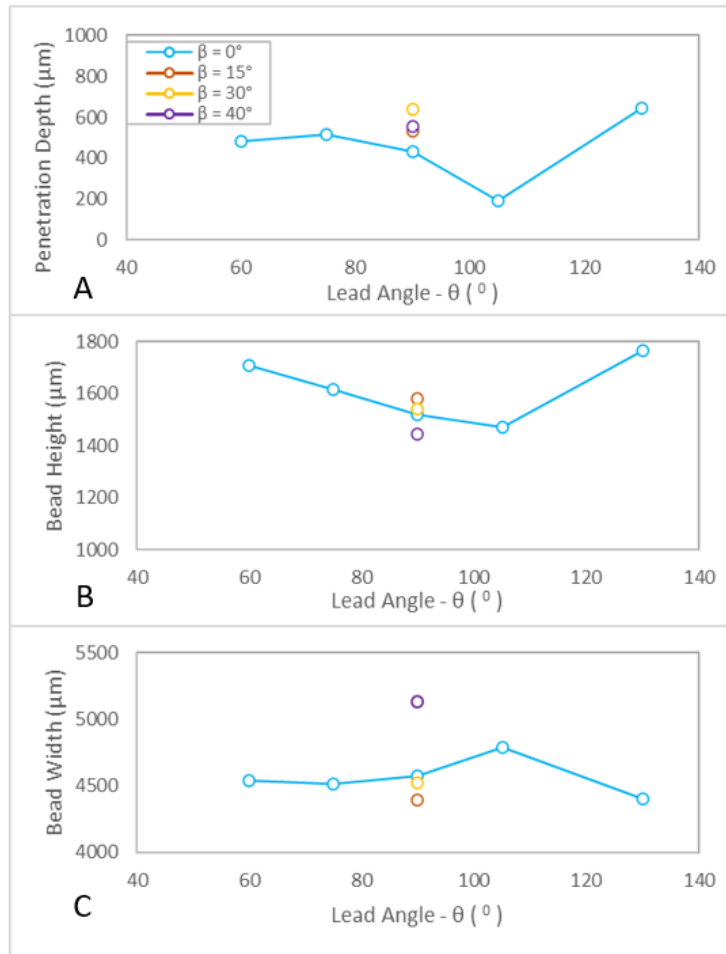


**Figure 13.** Effect of lead and lean angles on the bead morphology in the wire-feed DED method depositions.

Figure 14A illustrates the microstructure of the  $[\Theta = 105^\circ, \beta = 0^\circ]$  pure lead sample. Figures 14B to 14D show higher magnification images of the top, bottom, and center of the bead to examine the bead's solidification fronts. Columnar and equiaxed dendrites separated by columnar to equiaxed transition (CET zones) are observed. Fine columnar dendrites were observed predominantly towards the center of the beads, as shown in Figure 14D. On the other hand, these columnar dendrites transition to equiaxed dendrites around the bead edges, as shown in Figures 14B and 14C.

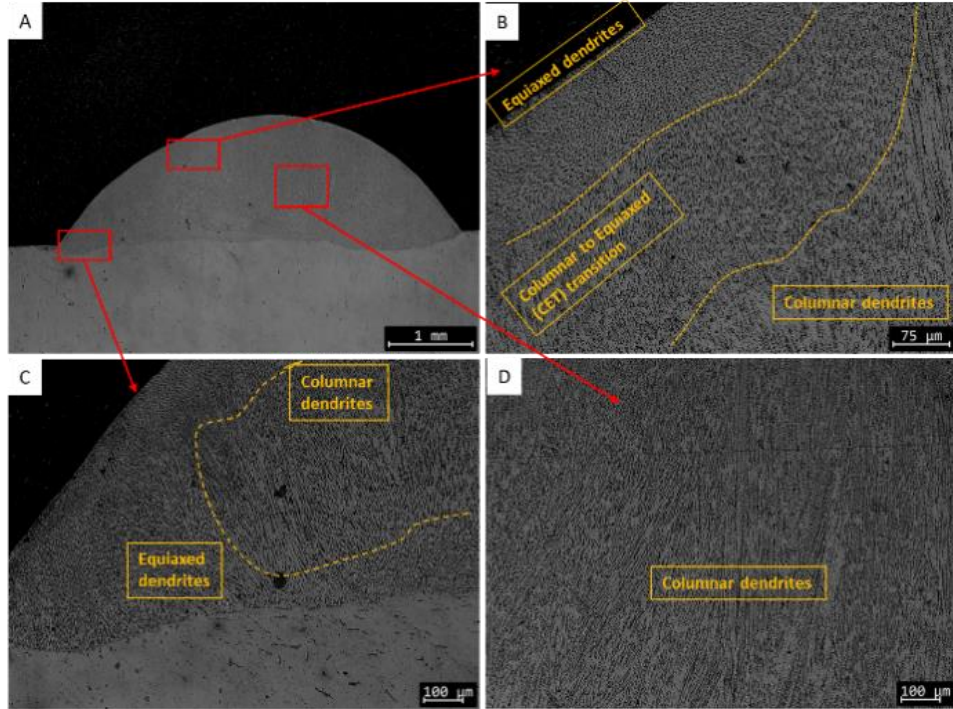


**Figure 14.** [A] Micrograph of the  $[\Theta = 105^\circ, \beta = 0^\circ]$  pure lead sample. High magnification images showing the grain structure at the [B] top, [C] bottom, and [D] center of the bead.

#### 4 Discussion

As shown in Figure 4, penetration depth experienced a drop with exceedingly non-orthogonal configurations, which can be due to the absolute distance traveled by the laser into the substrate. In an orthogonal setting, the penetration depth is at its maximum. However, with exceedingly non-orthogonal configurations, the laser travel trajectory is increasingly diagonal to the substrate surface, resulting in a reduced absolute penetration depth. Such phenomena have been observed in pulse laser welding of stainless steel [15]. This can be advantageous since this can reduce the remelted and recrystallized regions in previously deposited layers, resulting in a less complex/involved thermal history for the deposited material. The observed asymmetry, especially in less extreme non-orthogonal deposition samples, can indicate the presence of some of the underlying heat transfer phenomena. For acute lead angles, the laser power not only transfers to the substrate but also to the previously deposited material, thus dissipating the effective energy reaching the surface to a larger volume as compared to the obtuse lead angle deposition samples, which have the laser power mainly transferring to the substrate (refer to Figure 1 for better visualization).

Bead height and width also experienced a drop with more extreme non-orthogonal deposition, as shown in Figure 4. Powder catchment efficiency seemed to play an integral role here. During deposition, powder particles hit the melt pool and float momentarily before melting [16]. With a continuous powder flow, a large number of particles impact the already floating particles, thus experiencing a ricochet effect. Therefore, the resultant partially and/or non-melted particles are the primary reason for spatter along deposition edges and powder cloud formations, respectively [17]. The bounce-back angle will depend on the impact angle, which depends on the coaxial nozzle design. However, with exceedingly non-orthogonal angles, the bounce-back angle increases, reducing the laser-matter interaction time, thus reducing powder catchment efficiency.

The interaction time between the laser and the powder particles is directly related to the probability of these particles experiencing full, partial, or no melting. This outcome is primarily governed by the distance traveled within the laser's line of action. In other words, the longer a powder particle spends within the laser beam's line of action, the more energy it absorbs, and thus the propensity of its melting increases. For lead angles under  $90^\circ$ , as shown in Figure 1, as the particles ricochet off the substrate, they are met with a 'barrier' of the previously deposited material. As a result, some deflected particles are brought back into the melt-pool, slightly enhancing powder catchment efficiency. This could explain the observed asymmetry in the results obtained.

For a pure lean angle of  $45^\circ$ , shown in Figure 4, all bead metrics were the lowest, indicating that powder catchment efficiency was the least efficient in that angular configuration. This can be due to the excessive ricochet effect that occurs here, especially at such an extreme angle. Austenitic FCC phases were observed in both processed and unprocessed samples, as expected. However, no other phases were detected in this experiment, as compared to the delta ferrite detected in Costello et al. [18]. This can be explained by the integral role the alloying elements play in austenite stabilization. Manganese content here was around 1 wt%, which, coupled with the  $\sim 18$  wt% chromium presence, acts as an austenite stabilizer, as compared to becoming a ferrite stabilizer in the 5-8 wt% range [19]. Furthermore, the presence of Ni in high concentrations ( $\sim 13\%$ ) also promotes austenite stabilization. Thus, with the significant presence of austenite stabilizers, the presence of austenitic FCC phases seems valid in this experiment.

The diffraction peak patterns were equivalent, indicating that the general phase composition did not change with processing and varying angular configurations. Slight peak broadening was also observed, which can be attributed to the presence of residual stress (typically observed in additively manufactured materials), while the high peaks in the 111 and 200 planes point to textural representation within the material. The slight differences in diffraction patterns between the unprocessed and processed materials can stem from two possibilities. First, during processing, carbide and/or precipitate formations which are common in 316L austenitic stainless steels, especially  $M_{23}C_6$  carbides, could have occurred during the heating and re-heating of the material as one track is deposited next to the other to form the single layer [20]. Slight peak broadening was also observed, which can be attributed to the presence of residual stress, typically observed in additively manufactured materials, as well as the texture representation within the material.

The orientation distribution function results show that a visible fiber texture was present in the processed samples. Specifically, the fiber texture can be seen with consistently high intensities at  $\phi = 60^\circ$ ,  $\phi_2 = 45^\circ$ , and all  $\phi_1$  values. This can represent the elongated columnar and dendritic formations that are endemic to the rapid solidification phenomena observed in this process. Some visible texture with high intensities was also present in the  $\phi_2 = 15^\circ$ ,  $45^\circ$ , and  $75^\circ$  plots. These can represent the remainder equiaxed and cellular grain and sub-grain orientations that represent the general microstructural demographic of AM samples. Epitaxial growth can explain the reason behind the heavily fibrous texture representation observed in this process and this has been usually observed in additively manufactured materials [21]. No observable differences between samples were detected, though.

Similar solidification fronts were observed in examined samples of moderate non-orthogonal configurations. They all exhibited a radial symmetry which originated in the top center region of the beads. Columnar structures were detected at the outer edges of the bead, more specifically at the bead-substrate interface, while more equiaxed and cellular structures / sub-grains were observed closer to the center of the beads. This can possibly be due to slightly elevated

solidification rates as the heat transfer is directed radially outwards towards the substrate. Such solidification microstructure is a common observance in DED-processed materials [22].

For more extreme non-orthogonal depositions where penetration depths were very shallow, it can be observed that columnar structures dominated the microstructure. This can be due to the reduced substrate-bead interface perimeter as compared to samples with a larger penetration depth and thus a larger interface perimeter due to the circular shape of the perimeter. With a reduced perimeter, the heat-sinking effect of the substrate was diminished, therefore reducing the solidification rates experienced and thus only producing columnar structures, irrespective of the bead heights and widths involved. This highlights the primary role penetration depth plays in solidification phenomena during deposition.

In the wire-DED comparative study, the dilution region was preferentially positioned away from the bead center in the pure lead (right of the bead center) and pure lean (left of the bead center) configurations. Such dilution profile variations can be attributed to variations in the maximum laser intensity location within the melt-pool. It can also be attributed to the variations in laser intensity and wire location within the elongated laser beam diameter in non-orthogonal configurations. The observed asymmetry in the orthogonal configuration can be attributed to the wire feed not being consistently straight as it exits the contact tip, moreover the contact tip is  $16^\circ$  off to the normal that can add variability feed at exit of contact tip. Further examination of this phenomenon is warranted for future studies. A significantly different dilution profile was observed in the  $[\Theta = 105^\circ, \beta = 0^\circ]$  pure lead angle configuration. Maximum penetration, though relatively small, was observed towards the rightmost and leftmost corners of the bead. Such a penetration depth profile is observed in AM samples exhibiting a sickle-like temperature distribution on the surface of the melt-pool, typically resulting when process parameters exceed the evaporation temperature of the material. Consequently, the minimum penetration depth is observed at the center due to a comparatively lower temperature due to this sickle-like temperature distribution profile [23]. This indicates that this angular configuration represents a potential upper limit from a process-structure relation standpoint.

The observed Bell (bead width) and inverse Bell curve (bead height, penetration depth) behavior for the geometric characteristics, with the maximum and minimum points (respectively) at a lead angle of  $105^\circ$  indicates that there is an ability to adjust bead geometry by modifying lead angle. Note that, unlike powder-feed systems, wire-feed systems exhibit very high material retention efficiency within the melt-pool. Consequently, samples processed with equivalent laser energy densities and wire feed rates should result in highly similar volumetric bead geometries. This can be compared to powder-DED, which produced samples with progressively diminished bead geometries with more extreme non-orthogonal angular configurations.

## 5 Conclusions

This study examined the effects of laser incidence angle on bead morphology, phase composition, textural representation, bead microstructure, and resultant power losses. The following conclusions were resultant:

1. The ricochet effect, extent of absorbed reflected energy, and resultant powder catchment efficiency play an integral role in bead geometry generation. Acute lead angles exhibited more prominent characteristics due to the presence of the previously deposited material in the wake of the deposition front, acting as a barrier to ricocheted particles and thus enhancing powder catchment.

2. A larger lean angle, irrespective of the lead angle, resulted in smaller bead deposits. Furthermore, a pure lean angle of 45° resulted in significantly smaller bead sizes due to the greatly diminished powder catchment efficiency.
3. Austenitic FCC phases were observed in both unprocessed powders and the processed samples, with diffraction patterns exhibiting potential texture in the 111 and 200 planes and some peak broadening representative of residual stress present in the samples. Minor differences between the samples were observed, though.
4. Significant fibrous and other localized textures were present, indicating the presence of columnar/dendritic and equiaxed/cellular structures, respectively. Minor textural differences between samples were observed.
5. No significant differences in microstructural composition or grain size were detected with varying incidence angles at moderate non-orthogonal angles. Equivalent solidification microstructure was observed, with grain size variations remaining within the 1-1.5 $\mu$ m and 2-2.5 $\mu$ m ranges both within and across beads, respectively.
6. Penetration depth plays an integral role in the governing solidification phenomena, and consequent microstructure, with shallow penetration depths (<20 $\mu$ m) resulting in predominantly columnar structures form due to a reduced bead-substrate interface perimeter and thus less pronounced heat sinking effect by the substrate, irrespective of the bead heights and/or widths. In contrast, deeper penetration depths  $r$  in columnar structures to form at the interface, while more equiaxed structures form at the bead center.
7. Dilution profiles were found to be asymmetric in both orthogonal and non-orthogonal wire DED samples.
8. No significant microstructural differences were observed between powder-fed and wire-fed samples, indicating that similar solidification phenomena govern both hybrid manufacturing techniques.

## 6 Acknowledgments

We would also like to thank the Department of Energy for funding this work via DE-EE0008303. This work was supported by the US Department of Energy, Office of Energy Efficiency and Renewable Energy, Advanced Manufacturing Office under contract number DE-AC05-00OR22725. The authors would like to acknowledge the cooperation and support of the Mazak Corporation, and Autodesk. The authors would also like to acknowledge, Dennis Brown, and Matt Sallas for their contributions.

## 7 References

- [1] Zhu, Z., V. G. Dhokia, A. Nassehi, and S. T. Newman. "A Review of Hybrid Manufacturing Processes – State of the Art and Future Perspectives." *International Journal of Computer Integrated Manufacturing* 26, no. 7 (July 1, 2013): 596–615. <https://doi.org/10.1080/0951192X.2012.749530>
- [2] Wilson, J. Michael, Cecil Piya, Yung C. Shin, Fu Zhao, and Karthik Ramani. "Remanufacturing of Turbine Blades by Laser Direct Deposition with Its Energy and Environmental Impact Analysis." *Journal of Cleaner Production* 80 (October 1, 2014): 170–78. <https://doi.org/10.1016/j.jclepro.2014.05.084>

[3] Elser, Anja, Michael Königs, Alexander Verl, and Michael Servos. "On Achieving Accuracy and Efficiency in Additive Manufacturing: Requirements on a Hybrid CAM System." *Procedia CIRP*, 51st CIRP Conference on Manufacturing Systems, 72 (January 1, 2018): 1512–17. <https://doi.org/10.1016/j.procir.2018.03.265>

[4] Kumbhar, N. N., and A. V. Mulay. "Post Processing Methods Used to Improve Surface Finish of Products Which Are Manufactured by Additive Manufacturing Technologies: A Review." *Journal of The Institution of Engineers (India): Series C* 99, no. 4 (August 1, 2018): 481–87. <https://doi.org/10.1007/s40032-016-0340-z>.

[5] Lasemi, Ali, Deyi Xue, and Peihua Gu. "Recent Development in CNC Machining of Freeform Surfaces: A State-of-the-Art Review." *Computer-Aided Design* 42, no. 7 (July 1, 2010): 641–54. <https://doi.org/10.1016/j.cad.2010.04.002>

[6] Kim, Min-seob, Wook-jin Oh, Gyeong-yoon Baek, Yeong-kwan Jo, Ki-yong Lee, Sang-hu Park, and Do-sik Shim. "Ultrasonic Nanocrystal Surface Modification of High-Speed Tool Steel (AISI M4) Layered via Direct Energy Deposition." *Journal of Materials Processing Technology* 277 (March 1, 2020): 116420. <https://doi.org/10.1016/j.jmatprotec.2019.116420>

[7] Lin, Jiehming. "Laser Attenuation of the Focused Powder Streams in Coaxial Laser Cladding." *Journal of Laser Applications* 12, no. 1 (January 18, 2000): 28–33. <https://doi.org/10.2351/1.521910>

[8] Grasso, M., A. G. Demir, B. Previtali, and B. M. Colosimo. "In Situ Monitoring of Selective Laser Melting of Zinc Powder via Infrared Imaging of the Process Plume." *Robotics and Computer-Integrated Manufacturing* 49 (February 1, 2018): 229–39. <https://doi.org/10.1016/j.rcim.2017.07.001>

[9] Fu, Yunchang, A. Loredo, B. Martin, and A. B. Vannes. "A Theoretical Model for Laser and Powder Particles Interaction during Laser Cladding." *Journal of Materials Processing Technology* 128, no. 1 (October 6, 2002): 106–12. [https://doi.org/10.1016/S0924-0136\(02\)00433-8](https://doi.org/10.1016/S0924-0136(02)00433-8)

[10] Liu, Jichang, Lijun Li, Yuanzhong Zhang, and Xiaozhu Xie. "Attenuation of Laser Power of a Focused Gaussian Beam during Interaction between a Laser and Powder in Coaxial Laser Cladding." *Journal of Physics D: Applied Physics* 38, no. 10 (May 21, 2005): 1546–50. <https://doi.org/10.1088/0022-3727/38/10/008>

[11] Pinkerton, Andrew J. "An Analytical Model of Beam Attenuation and Powder Heating during Coaxial Laser Direct Metal Deposition." *Journal of Physics D: Applied Physics* 40, no. 23 (November 2007): 7323–7334. <https://doi.org/10.1088/0022-3727/40/23/012>

[12] Hao, Jingbin, Qingdong Meng, Congcong Li, Zhixiong Li, and Dazhong Wu. "Effects of Tilt Angle between Laser Nozzle and Substrate on Bead Morphology in Multi-Axis Laser Cladding." *Journal of Manufacturing Processes* 43 (July 2019): 311–22. <https://doi.org/10.1016/j.jmapro.2019.04.025>

[13] Abrams, Halle. "Grain Size Measurement by the Intercept Method." *Metallography* 4, no. 1 (February 1, 1971): 59–78. [https://doi.org/10.1016/0026-0800\(71\)90005-X](https://doi.org/10.1016/0026-0800(71)90005-X)

[14] Macken Instruments, Inc. "P2000Y." Accessed July 19, 2020. <https://www.macken.com/products/p2000y>

[15] Liao, Yi-Chun, and Ming-Huei Yu. "Effects of Laser Beam Energy and Incident Angle on the Pulse Laser Welding of Stainless Steel Thin Sheet." *Journal of Materials Processing Technology* 190, no. 1 (July 23, 2007): 102–8. <https://doi.org/10.1016/j.jmatprotec.2007.03.102>.

[16] Haley, James C., Julie M. Schoenung, and Enrique J. Lavernia. "Observations of Particle-Melt Pool Impact Events in Directed Energy Deposition." *Additive Manufacturing* 22 (August 1, 2018): 368–74. <https://doi.org/10.1016/j.addma.2018.04.028>.

[17] Siva Prasad, Himani, Frank Brueckner, and Alexander F. H. Kaplan. "Powder Incorporation and Spatter Formation in High Deposition Rate Blown Powder Directed Energy Deposition." *Additive Manufacturing* 35 (October 1, 2020): 101413. <https://doi.org/10.1016/j.addma.2020.101413>.

[18] Costello, Aaron C., Santhosh K. Koduri, and James W. Sears. "Optimization of Laser Powder Deposition for 316L Stainless Steel." *International Congress on Applications of Lasers & Electro-Optics* 2003, no. 1 (October 1, 2003): 701. <https://doi.org/10.2351/1.5060072>

[19] Shuro, I., S. Kobayashi, T. Nakamura, and K. Tsuzaki. "Determination of  $\alpha/\gamma$  Phase Boundaries in the Fe–Cr–Ni–Mn Quaternary System with a Diffusion-Multiple Method." *Journal of Alloys and Compounds* 588 (March 5, 2014): 284–89. <https://doi.org/10.1016/j.jallcom.2013.11.095>.

[20] Lee, J. H., and Y. S. Kim. "Intergranular Corrosion of 316L Stainless Steel by Aging and UNSM (Ultrasonic Nano-crystal Surface Modification) treatment." *Corrosion Science and Technology* 14, no. 6 (2015): 313–24. <https://doi.org/10.14773/cst.2015.14.6.313>.

[21] Basak, Amrita, and Suman Das. "Epitaxy and Microstructure Evolution in Metal Additive Manufacturing." *Annual Review of Materials Research* 46, no. 1 (2016): 125–49. <https://doi.org/10.1146/annurev-matsci-070115-031728>.

[22] Saboori, Abdollah, Donato Gallo, Sara Biamino, Paolo Fino, and Mariangela Lombardi. "An Overview of Additive Manufacturing of Titanium Components by Directed Energy Deposition: Microstructure and Mechanical Properties." *Applied Sciences* 7, no. 9 (September 2017): 883. <https://doi.org/10.3390/app7090883>.

[23] Zhong, Chongliang, Norbert Pirch, Andres Gasser, Reinhart Poprawe, and Johannes Henrich Schleifenbaum. "The Influence of the Powder Stream on High-Deposition-Rate Laser Metal Deposition with Inconel 718." *Metals* 7, no. 10 (October 2017): 443. <https://doi.org/10.3390/met7100443>.